

See discussions, stats, and author profiles for this publication at: <https://www.researchgate.net/publication/357323542>

Automatic Diagnosis of Different Grades of Diabetic Retinopathy and Diabetic Macular Edema Using 2D-FBSE-FAWT

Article in IEEE Transactions on Instrumentation and Measurement · December 2021

DOI: 10.1109/TIM.2022.3140437

CITATIONS

14

READS

262

2 authors:



Pradeep Kumar Chaudhary

Indian Institute of Technology Indore

10 PUBLICATIONS 134 CITATIONS

[SEE PROFILE](#)



Ram Bilas Pachori

Indian Institute of Technology Indore

296 PUBLICATIONS 12,147 CITATIONS

[SEE PROFILE](#)

Some of the authors of this publication are also working on these related projects:



Identification of epileptic seizures from scalp EEG signals based on TQWT [View project](#)



PhD work [View project](#)

Automatic Diagnosis of Different Grades of Diabetic Retinopathy and Diabetic Macular Edema Using 2D-FBSE-FAWT

Pradeep Kumar Chaudhary and Ram Bilas Pachori *Senior Member, IEEE*

Abstract—Diabetic retinopathy (DR) and diabetic macular edema (DME) are the two most common causes of blindness. The proposed work uses the order-zero and order-one two-dimensional Fourier-Bessel series expansion-based flexible analytic wavelet transform (2D-FBSE-FAWT) methods to diagnose different DR and DME grades. The comparison of different subband grouping methods are studied in this paper based on classification performance. Statistical features of the local binary pattern and its rotation invariant variance are used in the study. For classification purposes, random forest, k-nearest neighbors, and support vector machine are used. The Indian diabetic retinopathy image dataset (IDRiD) and Messidor database are used to evaluate the proposed method. Average accuracy (ACY_{avg}) measures have been considered for performance comparison. For IDRiD, ACY_{avg} obtained for DR and DME is 0.955 and 0.965, respectively. For the Messidor database, ACY_{avg} is 0.975 for DR and 0.985 for DME. For diagnosis of different grades of DR and DME, the best tuned parameters for designing order-zero 2D-FBSE-FAWT filter banks are level of decomposition = 3, Q-factor= 3, dilation factor = 0.5, and redundancy = 1.

Index Terms—Diabetic retinopathy, Diabetic macular edema, 2D-FBSE-FAWT, Local binary pattern, Fundus image.

I. INTRODUCTION

DIABETIC retinopathy (DR) and diabetic macular edema (DME) are eye complications whose root cause is diabetes. DR is developed when the blood vessel of the retina damages due to high blood sugar levels. Due to the damage, fluids like microaneurysms, haemorrhages, hard exudates, and soft exudates leak from blood vessels and get accumulated in eye (corresponding lesions are marked in fundus image [1]). The grade of DR can be characterised based on the volume of these fluids in fundus image. When these leaked fluids from a damaged blood vessel accumulate near to the macula region, it causes a vision problem [2]. This complication due to DR is known as DME. The grade of DME is based on the distance between hard exudates and macula. Both abnormalities, if left untreated, it may lead to permanent vision loss. The study [1] shows that on-time treatment of DR reduces the severity of vision loss by 90%. For that, there is a need for regular check-up of all patients who are suffering from diabetes. Hence, automated screening system is required for fast and efficient testing.

Pradeep Kumar Chaudhary and Ram Bilas Pachori are with Department of Electrical Engineering, Indian Institute of Technology Indore, Indore - 453552, India, (Email: phd1801202005@iiti.ac.in, pachori@iiti.ac.in)

Earlier, the methods used for the diagnosis of different grades of DR and DME were based on feature extraction from segmented blood vessels and abnormalities (area of exudates, neovascularization, microaneurysm, etc.) for DR grade [3] and features like the distance between exudates and macula after localizing macular region and exudates segmentation [4] for DME diagnosis. These methods are pixel-based approaches whose performance is easily affected by the low contrast of the image. Another popular method used for automatic diagnosis of different grades of DR and DME is a convolutional neural network (CNN) based approach. Several works have been carried out for the diagnosis of different grades of DR and DME separately like, for DR grading: Islam *et al.* [5] used heavy augmentation for automatic diagnosis, Lin *et al.* [6] used local feature by first extracting lesion information and then fused it with the original image. Similarly, for DME grading: Ren *et al.* [7] proposed semi-supervised graph-based learning, Syed *et al.* [8] used knowledge of local information related to macula and exudates region. There has been significantly less work done for joint diagnosis of different grades of DR and DME. Krause *et al.* [9] used Inception-V4 for diagnosis of different grades of DR and DME. Li *et al.* [1] used CANet for joint DR and DME grading using fused features of DR and DME. The problem with CNN-based approaches is that if CNN is to be trained from scratch, it will require high computational time and large database for proper tuning of the model parameters. Transfer learning can be the solution, but the size of the image has to be downsampled (or resized) depending on the type of pretrained network used. It will adversely affect the resolution and texture information present, as a result classification performance will be deteriorated [10]. In [11], signal decomposition technique along with machine learning is used for automated diagnosis of DR from fundus image where downsampling is not a necessary step. Additionally, by varying the level of decomposition we can retrieve texture information at different frequency scales. These types of methods are computationally efficient and neither require an extensive database nor a highly configured system.

Discrete wavelet transform (DWT) has significantly contributed to medical image processing, but since DWT is a dyadic decomposition method, it provides low Q-factor (QF). Short-time Fourier transform, cosine modulated filter-banks, and wavelet packet transform (WPT) are some other transforms used for oscillatory-type signals analysis. Nevertheless, these transforms do not provide flexibility to control QF. Tunable-Q wavelet transform (TQWT) [12] and flexible ana-

lytic wavelet transform (FAWT) [13] form a family of wavelet transform which have the flexibility to tune QF according to application. TQWT allows an easy way to select QF and redundancy (RDY). However, for a given QF and RDY, TQWT does not provide flexibility to select the desired dilation factor (DF). FAWT splits the high pass channel into negative and positive frequency parts, which allows the selection of an arbitrary sampling rate in a high-frequency channel. So, QF, RDY, and DF can be easily selected in FAWT which makes it a flexible transform. In [14], the authors have proposed Fourier-Bessel series expansion (FBSE) based FAWT (FBSE-FAWT), where FBSE spectrum is used for the implementation of FAWT instead of Fourier spectrum. FBSE represents signal only in terms of positive frequencies; therefore, it makes the implementation process easier, as the high pass channel will no longer require two separate filter-banks for positive and negative frequency parts [14]. The FAWT and FBSE-FAWT have been found effective in signal processing tasks [14]. Similarly, the two-dimensional (2D) version of FBSE-FAWT (2D-FBSE-FAWT) may be well suitable for images with texture variations. The above idea motivated us to explore 2D-FBSE-FAWT for image analysis. In our previous works [15], [16], we have explored both order-zero and order-one FBSE for analysis of fundus images. The results motivated us to use both order-zero and order-one versions of 2D-FBSE-FAWT for fundus image analysis.

We also analyzed the effect of different subband grouping operations, namely, 10-channel, 7-channel, and 4-channel (for three levels of decomposition) [17]. These operations will give rotational invariant features. For feature extraction from grouped subband images at a different scale of 2D-FBSE-FAWT, histogram features of the local binary pattern (LBP) and rotation invariant variance (VAR) are used.

In recent years, texture analysis through LBP has been used in various applications, including medical images. For fundus images, LBP is used in applications like blood vessel extraction [18], for glaucoma detection [19], and even used for diagnosis of DR and macular edema (ME). LBP with VAR features [20] is used for three-class classification, namely, DR, ME, and healthy subject. Garnier et al. [21] investigated LBP at a different scale of DWT to diagnose ME. Due to the use of LBP features, these methods have bypassed the lesion segmentation step, which is conventionally used for DR and DME detection. Inspired by this, we have investigated LBP and VAR histogram features at different scales of 2D-FBSE-FAWT.

The main contributions of the work are as follows:

- Introduces order-zero and order-one 2D-FBSE-FAWT for image decomposition.
- Selection of best QF, RDY, and DF for the application of diagnosis of different grades of DR and DME.
- LBP and VAR features are investigated at different scales of 2D-FBSE-FAWT.
- Study is also performed to find the best grouping operation of subband images.

The remaining paper is organized as follows: Section II describes the database used and 2D-FBSE-FAWT method in brief. In Section III, the methodology for the diagnosis

TABLE I: Description of the studied databases.

Database	Disease-grades	Remark	Count
IDRiD (516 images) [4288 × 2848]	DR-0	No DR	168
	DR-1	Mild	25
	DR-2	Moderate	168
	DR-3	Severe	93
	DR-4	Proliferative DR	62
	DME-0	No DME	222
	DME-1	D > One papilla diameter	51
	DME-2	D ≤ One papilla diameter	243
Messidor (1200 images) [variable size]	DR-0	No DR	546
	DR-1	0 < NMA < 5 and NH = 0	153
	DR-2	5 < NMA < 15 or 0 < NH < 5 and NNV = 0	247
	DR-3	NMA ≤ 5 or NH ≥ 5 or NNV = 1	254
	DME-0	No DME	974
	DME-1	D > One papilla diameter	75
	DME-2	D ≤ One papilla diameter	151
	APOTOS-19 (3662 images) [variable size]	No DR	1805
APOTOS-19 (3662 images) [variable size]	DR-1	Mild	370
	DR-2	Moderate	999
	DR-3	Severe	193
	DR-4	Proliferative DR	62

NOTE: NMA= Number of microaneurysm, NH= Number of hemorrhage, NNV= 1 for presence or 0 for absence of neovascularization, and D=Distance between lesions and macula.

of different grades of DR and DME is explained. Results are discussed in Section IV. Finally, Section V provides the conclusion of the work.

II. DATABASE AND 2D-FBSE-FAWT METHOD

A. Database

In this work, total three databases have been used namely, Indian diabetic retinopathy image dataset (IDRiD) [22] (413 training images and 103 test images), Messidor [23], and Asia Pacific Tele-Ophthalmology Society (APOTOS) 2019 database. Detail of each database is shown in Table I. The remark in table shows the criteria considered by the databases for grading DR and DME. APTOS database can be downloaded from <https://www.kaggle.com/c/aptos2019-blindness-detection/overview>. Fig. 1 shows different grades of DR and DME in IDRiD database.

B. 2D-FBSE-FAWT method

FBSE transforms signal from spatial domain (m, n) to order (k_1, k_2) domain. Generalized mathematical expression of order- A 2D-FBSE for image $I(m, n)$ of size $M \times N$ can be expressed as follows [24]–[26]:

$$I(m, n) = \sum_{k_1=1}^M \sum_{k_2=1}^N C(k_1, k_2) J_A\left(\frac{\varsigma_{k_2} n}{N}\right) J_A\left(\frac{\varsigma_{k_1} m}{M}\right) \quad (1)$$

Where m and n vary from 0 to $M - 1$ and 0 to $N - 1$, respectively, $J_A(\cdot)$ represents Bessel function of order A and term $C(k_1, k_2)$ is a FBSE coefficient at location (k_1, k_2) , and it can be expressed as,

$$C(k_1, k_2) = \frac{4}{\alpha} \sum_{m=0}^{M-1} \sum_{n=0}^{N-1} m n I(m, n) J_A\left(\frac{\varsigma_{k_2} n}{N}\right) J_A\left(\frac{\varsigma_{k_1} m}{M}\right) \quad (2)$$

Where $\alpha = (NM)^2 (J_{A-1}(\varsigma_{k_1}) J_{A-1}(\varsigma_{k_2}))^2$. Parameters ς_{k_1} and ς_{k_2} denote the k_1^{th} and k_2^{th} positive roots of equation $J_A(\cdot) = 0$. Here k_1 and k_2 represent index of row and column of FBSE coefficients. Where k_1 vary from 1 to M and k_2 vary

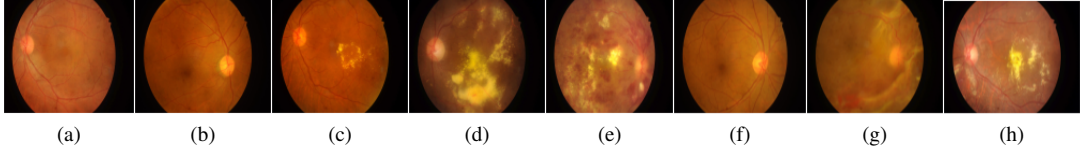


Fig. 1: Fundus images having DR of grade (a) 0, (b) 1, (c) 2, (d) 3, and (e) 4, and DME of grade (f) 0, (g) 1, and (h) 2.

TABLE II: Mathematical expressions of filter-banks.

General implementation	Easy implementation
$H(k_i) = \begin{cases} (pq)^{1/2}, & k_i < K_p \\ (pq)^{1/2}\theta\left(\frac{k_i - K_p}{K_s - K_p}\right), & K_p \leq k_i \leq K_s \\ 0, & k_i \geq K_s \end{cases}$	$LPF(k_i) = \begin{cases} 1, & k_i < pK_p \\ \theta\left(\frac{k_i - K_p}{K_s - K_p}\right), & pK_p \leq k_i \leq pK_s \\ 0, & k_i \geq pK_s \end{cases}$
$G(k_i) = \begin{cases} (rs)^{1/2}\theta\left(\frac{\pi - (k_i - K_0)}{K_1 - K_0}\right), & K_0 \leq k_i \leq K_1 \\ (rs)^{1/2}, & K_1 \leq k_i \leq K_2 \\ (rs)^{1/2}\theta\left(\frac{k_i - K_2}{K_3 - K_2}\right), & K_2 \leq k_i \leq K_3 \\ 0, & k_i \in [0, K_0] \cup (K_3, I) \end{cases}$	$HPF(k_i) = \begin{cases} \theta\left(\frac{\pi - (k_i - K_0)}{K_1 - K_0}\right), & rK_0 \leq k_i \leq rK_1 \\ 1, & rK_1 \leq k_i \leq rK_2 \\ \theta\left(\frac{k_i - K_2}{K_3 - K_2}\right), & rK_2 \leq k_i \leq rK_3 \\ 0, & k_i \in [0, rK_0] \cup (rK_3, I) \end{cases}$

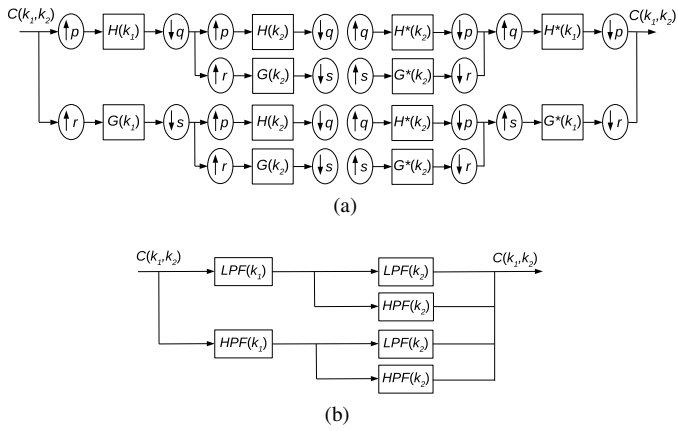


Fig. 2: (a)Analysis and synthesis filter-banks for implementation of 2D-FBSE-FAWT. and (b) Design of filter-bank for easy implementation of 2D-FBSE-FAWT.

from 1 to N . k_i can be directly expressed in terms of frequency ω_{k_i} , using the relation $k_i = \frac{\omega_{k_i} \times I}{\pi}$ [27].

Fig. 2(a) shows analysis and synthesis filter-banks for implementation of 2D-FBSE-FAWT. $H(k_i)$ and $G(k_i)$ are low pass and high pass filter-banks, whose mathematical expressions in terms of order k_i are shown in Table II, where $i=1$ for row operation and $i=2$ for column operation, $K_p = \frac{(1-\beta)I}{p} + \frac{\epsilon}{p}$, $K_s = \frac{I}{q}$, $K_0 = \frac{(1-\beta)I}{r} + \frac{\epsilon}{r}$, $K_1 = \frac{pI}{qr}$, $K_2 = \frac{I-\epsilon}{r}$, $K_3 = \frac{I+\epsilon}{r}$, $\epsilon = \frac{1}{32} \left(\frac{p-q-\beta q}{p+q} \right) I$, and $\theta(y) = \frac{1}{2}(1 + \cos(y))\sqrt{2 - \cos(y)}$ ($y \in [0, \pi]$). $I = M$ (number of row) or $I = N$ (number of column) depending on the direction in which filtering is performed.

In order to get desirable QF, RDY, and DF parameters, β and ϵ should follow constraints such as, $(1 - \frac{p}{q}) \leq \beta \leq \frac{r}{s}$ and $\epsilon \leq \frac{p-q-\beta q}{p+q}$ and $|\theta(\pi - y)| + |\theta(y)| = 1$, respectively. The condition for perfect reconstruction of filter-bank is $\frac{1}{pq} \left| H\left(\frac{k_i}{p}\right) \right|^2 + \frac{1}{rs} \left| G\left(\frac{k_i}{r}\right) \right|^2 = 1$ for $k_i \in [0, L]$. The mathematical expression for QF, RDY and DF in terms of

p , q , r , and s are as follows: $QF = \frac{2-\beta}{\beta}$, $RDY = (r/s) \frac{1}{1-p/q}$, $DF = \frac{p}{q}$.

The same implementation of 2D-FBSE-FAWT can also be performed in an easier way [13]. The mathematical expression of which is given in Table II, where $LPF(k_i)$ and $HPF(k_i)$ represent low pass filter and high pass filter, respectively. The equation can be obtained by using perfect reconstruction conditions and the general equation of 2D-FBSE-FAWT (Table II). Fig. 2(b) shows the filter-bank to implement 2D-FBSE-FAWT (equivalent to Fig. 2(a)).

III. METHODOLOGY

Block diagram of proposed work for diagnosis of different grades of DR and DME is shown in Fig. 3. In the pre-processing step, contrast of images is improved using contrast limited adaptive histogram equalization (CLAHE) [16].

After pre-processing, order- A 2D-FBSE-FAWT is used to decompose images into subband images. An issue with the wavelet decomposition methods is the selection of the number of decomposition levels (L). As L increases, the frequency resolution increases which is required for good discrimination between two images. However, it is also found that as the L increases, there is a decrease in classification performance. In earlier works [28], L is generally set between 3 to 5 (trial and error basis). Hence, there is a requirement of a technique to select a particular value of L . Here we have used FBSE energy (E_{FBSE}) based L selection which is defined as, $E_{FBSE} = \frac{E_{\text{Approximate component}}}{E_{\text{Original image}}}$, where, $E_{\text{Approximate component}}$ represents energy of approximate component at L^{th} level of decomposition and $E_{\text{Original image}}$ is energy of original image. Decomposition process is stopped when $E_{FBSE} < 0.05$ [28]. Once L is fixed, the number of subband images will be fixed.

In literature, it is also found that combining subband images in a particular manner has provided better performance [16]. In [16], the authors have combined subband images in three ways, namely, $(3L+1)$ channels, $(2L+1)$ channels, and $(L+1)$ channels. These grouping methods for $L = 3$ decomposition are shown in Fig. 4 i.e. 10-channel, 7-channel, and 4-channel.

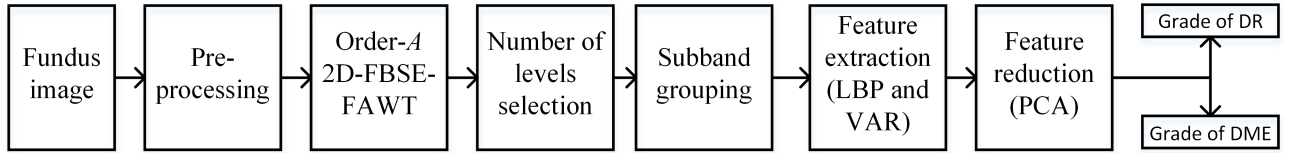


Fig. 3: Proposed framework for automated diagnosis of different grades of DR and DME.

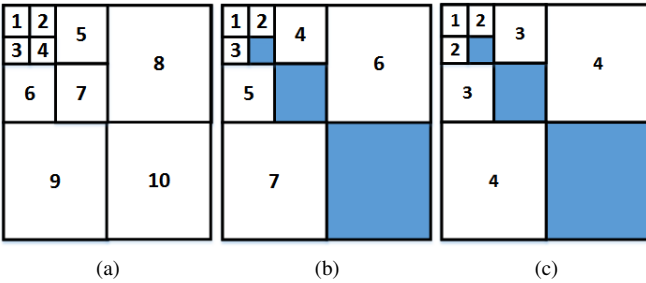


Fig. 4: (a) 10-channel, (b) 7-channel, and (c) 4-channel subband grouping for three-level of decomposition.

The dark portion in Fig. 4 are the subbands which are not included in the feature extraction and classification process. In this work, we have studied all three schemes to classify different grades of DR and DME.

For feature extraction, statistical features namely, mean, standard deviation, median, entropy, kurtosis, and skewness of LBP and VAR histogram are used [29]. LBP provides texture information and VAR provides contrast measure by defining rotation local variance. Mathematical expressions for LBP and VAR are as follows:

$$\text{LBP}_{U,V} = \sum_{u=1}^{U-1} T(f_u - f_c)2^u, \quad T(y) = \begin{cases} 1, & \text{if } y \geq 0 \\ 0, & \text{if } y \leq 0 \end{cases} \quad (3)$$

$$\text{VAR}_{U,V} = \frac{1}{U} \sum_{u=1}^{U-1} (f_u - \mu)^2, \quad \mu = \frac{1}{U} \sum_{u=1}^{U-1} f_u \quad (4)$$

Where U is the number of the pixel on the symmetric circular neighborhood of radius V . f_u is a value of neighborhood pixel around center pixel f_c . The number of the extracted features will depend on L and the type of subband combination is used. In general, it will be equal to $12 \times N \times 3$. Where 12 represents 6 LBP and 6 VAR statistical histogram features, 3 is the number of channels (R, G, and B), and N = number of subbands (depend on type of subband grouping and L). The extracted features are then pre-processed using data normalization and data resampling.

Principal component analysis (PCA) is then used to reduce the dimension of the feature by setting the cumulative sum of the principal component variance to 95% [16]. The reduced features are then passed through two classifiers separately. One classifier is used to classify different grades of DR and other for different grades of DME.

In this work, the classification learner application of MATLAB is used for classification purposes. Among 24 classifiers present in the application, k-nearest neighbors (KNN)

[30] and support vector machine (SVM) [31] show the best performances. Along with them, random forest (RF) [32] is also considered as it has also provided significantly improved performance in the proposed work. In this work number of decision trees is set to 100. For KNN classifier, number of neighbours is set equal to 1 and Euclidean distance as distance metric. The kernel function and scale for SVM classifier are set as Gaussian function and 0.28161. The parameters mentioned above are optimum parameters obtained by the optimizable KNN and SVM option present in the MATLAB, and for RF the best number of trees is obtained by trial and error method, keeping computational time and performance (as compared to SVM and KNN) in consideration.

IV. RESULTS

In this work, we evaluated proposed model using IDRiD. The simulation study has been carried out in three parts whose results are discussed in separate subsections. First part of the simulation study is for parameter selection of order-zero 2D-FBSE-FAWT filter-bank, namely, L , QF, RDY, and DF. In the second part of the simulation study, the performances of order-zero 2D-FBSE-FAWT subband grouping methods are compared. In third part of the simulation study, the performance of order-zero and order-one 2D-FBSE-FAWT methods are compared with different traditional wavelets, x-lets, transfer learning, and 2D-FBSE-based empirical wavelet transform (2D-FBSE-EWT) based methods. Finally, to check the robustness of the proposed methods, it is tested on the Messidor and APTOS databases. The performance parameter average accuracy ACY_{avg} ($\text{ACY}_{avg} = (\text{SEN}_{avg} + \text{SPE}_{avg})/2$) is used for selecting the 2D-FBSE-FAWT parameters for designing the filter-bank. Where SEN_{avg} and SPE_{avg} are calculated by averaging SEN and SPE of each grade of DR and DME [16]. In medical applications, it is preferred to have a model with higher SEN in medical applications, but it does not imply that the system can have low SPE. Also SEN and SPE are complementary parameters, so to avoid the confusion, ACY_{avg} is used.

To compare the proposed methodology for the diagnosis of different grades of DR and DME with other existing work in literature, joint accuracy (JAC) is used as a performance parameter. For calculating JAC, the counting is set to one if prediction and ground-truth label matches for both DR and DME; otherwise, zero [1].

A. Parameter selection

To illustrate parameter selection step, the order-zero 2D-FBSE-FAWT is considered for the simulation study. Compar-

TABLE III: Selected L , number of reduced features for each QF.

QF	L	Number of features	Reduced features
1	2	252	35
2	2	252	35
3	3	360	38
4	4	468	40
5	5	576	42

ison between order-zero and order-one 2D-FBSE-FAWT has been provided in third part of simulation study.

For setting L , FBSE energy based criteria is used for QF = 1 to 5. For this step, randomly 25 images are selected from each grade. After obtaining the L value, the best QF, RDY, and DF are selected based on ACY_{avg} . Once the best QF, RDY, and DF are selected, then order-zero 2D-FBSE-FAWT is used to decompose the image into subband images. From each subband image, six statistical histogram features from LBP and VAR histograms are calculated. PCA is used to reduce the dimension of the features. Table III shows the value of L , the number of features, and the number of reduced features obtained using PCA (95% cumulative variance) at each QF. Table IV shows the performance measures of the proposed method for QF=1 to 5. The RF, KNN, and SVM are used for classification with 5-fold cross-validation. Bold entries in the table show the best results of the proposed method. It is found that RF for DME ($\text{DME-ACY}_{avg} = 0.965$) and KNN for DR ($\text{DR-ACY}_{avg} = 0.935$) have provided better performance with $\text{QF}=3$ ($p=1$, $q=2$, $r=1$, and $s=2$). β is set to 1/2 to get the $\text{QF}=3$ and according to the relation $(1 - \frac{p}{q}) \leq \beta \leq \frac{r}{s}$, the $\frac{r}{s} \geq \frac{1}{2}$ and $\frac{p}{q} \geq \frac{1}{2}$.

Now, for the fixed QF, the best DF is selected. According to constraints $\frac{p}{q} \geq 0.5$ and $q \geq p$ the DF can vary between 0.5 to 1. The performance measures for $\text{QF}=3$ (fixed) and $\text{DF} = 0.5$, 0.6, 0.75, 0.8, and 1 are shown in Table IV. RF and KNN are used for classification purposes as both classifiers have given a better performance than SVM while selecting QF. Best results are obtained at $\text{DF} = 0.5$ and 0.6 for DR using KNN classifier ($(\text{DR-ACY}_{avg} = 0.935)$) and 0.5 for DME using RF classifier ($\text{DME-ACY}_{avg} = 0.965$). The DF is set to 0.5 because it has given the best performance for both cases. We also compare the proposed method for $\text{RDY} = 1$ to 5 for $\text{QF}=3$ and $\text{DF} = 0.5$ in the same table. The best results are obtained at $\text{RDY} = 1$ for DR using KNN classifier and 1 for DME using RF classifier. For both the cases best performance is obtained at $\text{RDY} = 1$ so, the best parameters for designing a filter-bank using 2D-FBSE-FAWT are $\text{QF}=3$, $\text{DF} = 0.5$, and $\text{RDY} = 1$. p , q , r , s , and L parameters are 1, 2, 1, 2, and 3, respectively.

B. Subband grouping methods

In the first part of simulation study, no subband grouping was performed, all 10 channels are used separately for feature extraction. For the parameters selected previously, features from 7-channel and 4-channel subbands have also been used to classify DR and DME grades. Table V shows the performance comparison of DR and DME for 10-channel, 7-channel, and 4-channel-based approaches. Entry in brackets represents the

number of reduced features used for each channel-based approach. Bold entries in the table show that the best ACY_{avg} is obtained for 7-channel based grouping method using RF classifier. The best ACY_{avg} for DR and DME is 0.955 and 0.965, respectively.

Fig. 5 shows R-, G-, B-channel, and RGB decomposed images obtained by 7-channel subband grouping operation. The red (hemorrhages, and neovascularization) and yellow (exudates) lesions present in the original images are highlighted with red and yellow boxes in the figure, respectively. Particular channels of the RGB image enhance the particular colors in the image, and the approximate component of each channel shows the smooth portion in the channel. So, the approximate (first) subband highlights the lesions present in the fundus image, like in B-channel approximate subband image highlights red lesions in images (shown with red box), G-channel approximate subband image highlights exudates in the image (shown with a yellow box). All other detail subband images highlight edges (high frequency) like blood vessels, exudates boundaries, and hemorrhages boundaries in the different orientations of the fundus image. The texture features extracted from such multiresolution images will be beneficial in the diagnosis of different grades of DR and DME.

Figs. 6 (a) and (b) show row and column filter-banks for selected parameters (i.e. $\text{QF}=3$, $\text{DF}=0.5$, $\text{RDY} = 1$, and $L=3$). To understand how by varying QF, RDY, DF, and L these texture information varies, the tuned row filter bank (shown in Fig. 6(a)) is compared with row filter-bank for $\text{QF}=3$, $\text{DF}=0.5$, $\text{RDY}=2$, and $L=3$ (shown in Fig. 6(c)) and row filter-bank for $\text{QF}=5$, $\text{DF}=0.5$, $\text{RDY} = 1$, and $L=5$ (shown in Fig. 6(d)). The filter-bank in Fig. 6(c) and Fig. 6(a) have same QF and DF but there RDY is different, and there is no variation found in bandwidth of filter-banks, just slight variations in transition bands, same can be verified with classification performance results in Table IV (slight variation in DR-ACY_{avg} and DME-ACY_{avg} in Table IV, RDY section, with $L=3$). The filter-banks in Fig. 6(d) and Fig. 6(a) have different QF and L , but same DF and RDY (see Table III). Due to different QF the bandwidth of the filter-banks are different, so the subband image obtained by both the filter-bank will have different texture information. The filter-bank with $\text{QF}=5$ will take more level of decomposition ($L=5$) and will use high dimensional features (576) to get approximately the same performance as obtained by filter-bank of Fig. 6(a) (see Table IV).

C. Performance comparison and robustness check

In this section, performance of order-zero and order-one 2D-FBSE-FAWT methods are compared with order-zero and order-one 2D-FBSE-EWT methods, wavelet transforms: DWT [33], dual-tree complex wavelet transform (DTCWT) [34], WPT [35], X-lets: wedgelet [36], curvelet [37], and contourlet [38], and transfer learning feature-based method. For wavelets and X-lets, the L and feature selection criteria are considered same as our proposed method i.e., energy-based criteria are used for scale selection in X-lets and L selections for wavelets, PCA is used for feature reduction followed by parameter

TABLE IV: Performance measures for different values of QF, DF, and RDY.

	QF=1 ($p = 2, q = 2, r = 2, s = 2$)			QF=2 ($p = 1, q = 3, r = 2, s = 3$)			QF=3 ($p = 1, q = 2, r = 1, s = 2$)			QF=4 ($p = 3, q = 5, r = 2, s = 5$)			QF=5 ($p = 2, q = 3, r = 1, s = 3$)		
	SVM	RF	KNN	SVM	RF	KNN	SVM	RF	KNN	SVM	RF	KNN	SVM	RF	KNN
DR-ACY _{avg}	0.910	0.910	0.920	0.900	0.925	0.925	0.930	0.915	0.935	0.915	0.910	0.920	0.920	0.925	0.925
DME-ACY _{avg}	0.935	0.950	0.945	0.930	0.945	0.940	0.935	0.965	0.955	0.940	0.960	0.960	0.955	0.950	0.950
	DF=0.5 ($p = 1, q = 2$)			DF=0.6 ($p = 2, q = 3$)			DF=0.75 ($p = 3, q = 4$)			DF=0.8 ($p = 4, q = 5$)			DF=1 ($p = 2, q = 2$)		
DR-ACY _{avg}	-	0.915	0.935	-	0.915	0.935	-	0.930	0.875	-	0.930	0.925	-	0.915	0.920
DME-ACY _{avg}	-	0.965	0.955	-	0.960	0.960	-	0.955	0.945	-	0.955	0.945	-	0.905	0.925
	RDY=1 ($r = 1, s = 2$)			RDY=2 ($r = 2, s = 2$)			RDY=3 ($r = 3, s = 2$)			RDY=4 ($r = 2, s = 1$)			RDY=5 ($r = 5, s = 2$)		
DR-ACY _{avg}	-	0.915	0.935	-	0.920	0.925	-	0.920	0.925	-	0.920	0.925	-	0.920	0.930
DME-ACY _{avg}	-	0.965	0.955	-	0.955	0.945	-	0.955	0.950	-	0.950	0.950	-	0.955	0.940

TABLE V: Performance measures for channel-10, channel-7 and channel-4 subband grouping methods.

	DR						DME					
	10-channel (38 feature)		7-channel (30 features)		4-channel (26 features)		10-channel (38 features)		7-channel (30 features)		4-channel (26 features)	
	RF	KNN	RF	KNN	RF	KNN	RF	KNN	RF	KNN	RF	KNN
ACY _{avg}	0.915	0.935	0.955	0.940	0.930	0.920	0.965	0.955	0.965	0.955	0.955	0.955

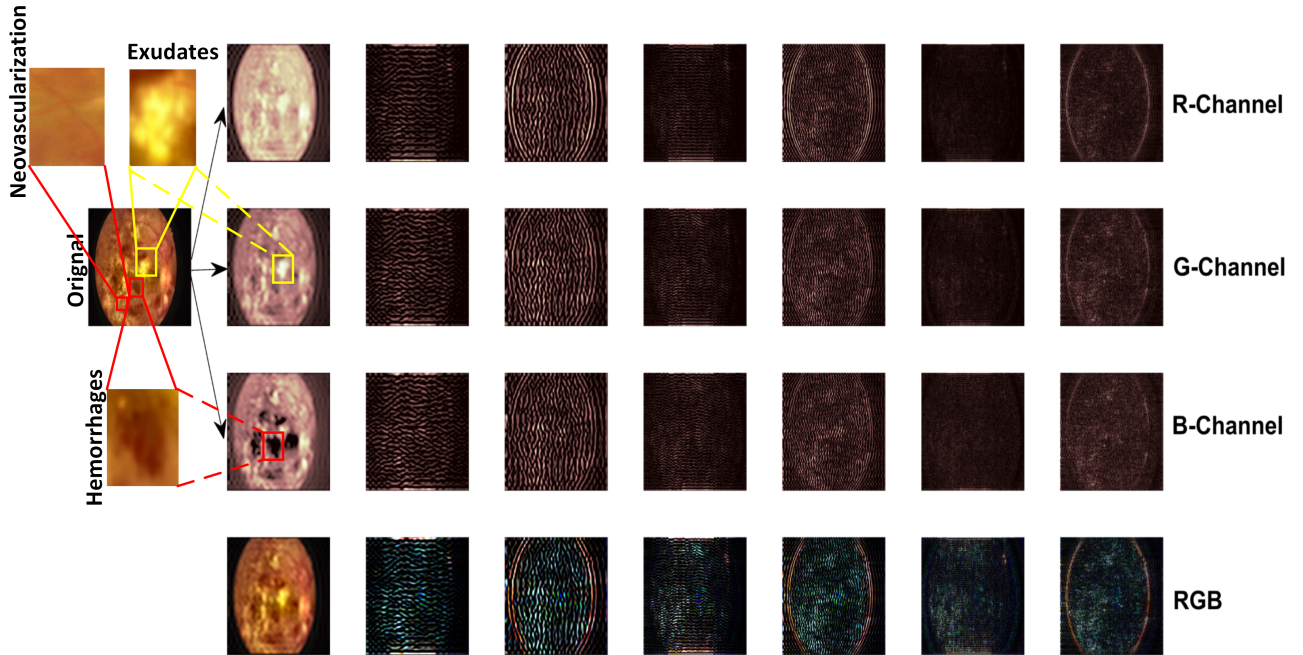


Fig. 5: 7-channel subband images for QF=3, dilation-factor=0.5, and RDY=1.

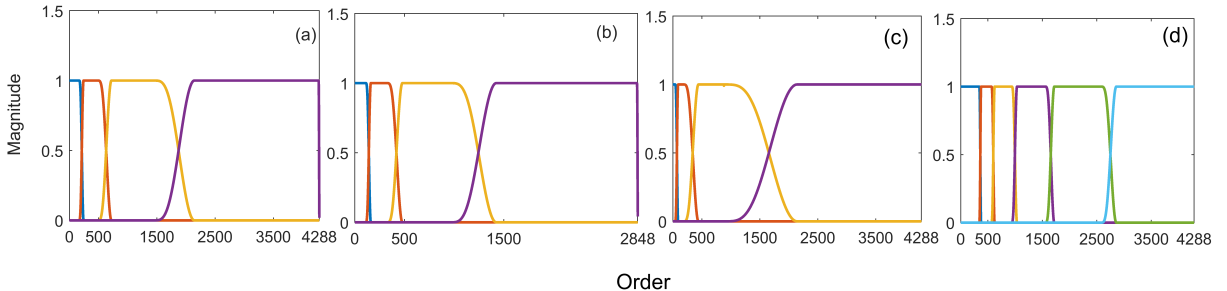
Fig. 6: (a) Row and (b) Column filter-bank for QF=3, DF=0.5, and RDY = 1. (c) Row filter-bank for QF=3, DF=0.5, RDY = 1, and $L=3$ and (d) Row filter-bank for QF=5, DF=0.5, RDY=1, and $L=5$.

TABLE VI: Performance comparison of proposed methods (order-zero and order-one 2D-FBSE-FAWT based methods) with different wavelets, x-let, 2D-FBSE-EWT, transfer learning, and without decomposition based methods.

Methods	Level of decomposition (L)	Feature after PCA	Other remark	ACY _{avg}		JAC	Time (s)
				DR	DME		
DWT	4 (Energy based selection)	43 (95% variance)	Mother wavelet: Haar 7-channel grouping	0.860	0.880	0.620	0.86
WPT	4 (Energy based selection)	60 (95% variance)	Mother wavelet: db-1 No grouping	0.880	0.910	0.640	1.18
DTCWT	4 (Energy based selection)	55 (98% variance)	Mother wavelet: Haar No grouping	0.900	0.920	0.650	0.985
Redeglet	4 (Energy based selection)	35(98%)	No grouping	0.932	0.38	0.69	0.86
Curvelet	Scale =4 (Energy based selection) Orientation=16 (Default)	80 (95%)	No grouping	0.952	0.938	0.72	1.08
Contourlet	Scale =4 (Energy based selection) $k =[1, 3, 4, 8, 16]$	104 (90%)	LFB=ladder structure PKVA filters DFB=ladder structure PKVA filters No grouping	0.950	0.942	0.71	1.10
No decomposition	-	11 (98% variance)	-	0.800	0.870	0.590	0.390
Transfer learning	-	-	-	0.920	0.890	0.700	0.780
Order-one 2D-FBSE-EWT	Nrow=Ncol=1	22 (98% variance)	-	0.905	0.920	0.690	0.982
Order-zero 2D-FBSE-EWT	Nrow=Ncol=1	22 (98% variance)	-	0.920	0.690	0.690	0.982
Order-one 2D-FBSE-FAWT	3 (Energy based selection)	30 (95% variance)	QF=3, DF=0.5, RDY=1, and 7-channel grouping	0.950	0.940	0.720	0.857
Order-zero 2D-FBSE-FAWT	3 (Energy based selection)	30 (95% variance)	QF=3, DF=0.5, RDY= 1, and 7-channel grouping	0.955	0.965	0.780	0.857

tuning. Tuned parameters like mother wavelets, orientation, type of grouping, and subband image at each scale (k in contourlet) are shown in Table VI. For 2D-FBSE-EWT, the number of row boundaries (Nrow) and the number of column boundaries (Ncol) are set to 1, as done by the authors in [16]. For the transfer learning-based method, pretrained ResNet-50 architecture is used. The reason behind choosing ResNet-50 architecture is that it has been used in a recent study as a backbone network for automatic diagnosis of different grades of DR and DME [1]. In the transfer learning feature-based method, the parameters are chosen to be Adam as optimizer, batch size=40, number of epochs=1000, initial learning rate = 0.003 and is decayed with cosine annealing for each batch (same as done in [1]). Random vertical and horizontal data augmentation was also performed. The performance of the proposed methodology is also compared with the method in which the decomposition method is skipped. Table VI shows the comparison of all the methodologies based on computational time for testing a single image, ACY_{avg} for DR and DME, and JAC.

The DWT and X-let transforms are constant-Q transforms and provide dyadic scale decomposition. So they will provide poor frequency resolution. As a result, these methods took more decomposition levels and computational time to provide approximately same performance as our proposed methodology.

The proposed framework has shown better performance than no decomposition based method and transfer learning-based method (which uses features which are obtained from the last layer of ResNet-50). This proves the effectiveness of using a multiresolution-based method for disease diagnosis.

Although, the 2D-FBSE-EWT method is an adaptive method, it fails to provide better performance compared to the proposed method. The reasons may be as follows: 1) since it is an adaptive method, it will provide different numbers of subband images for different images, 2) even slight variation due to edge or noise will give irrelevant boundaries in FBSE

plane. So for applying this method to any real-world problem, the number of boundaries has to be fixed, making the adaptive advantage irrelevant. Hence for the comparison of 2D-FBSE-EWT with the proposed method, Nrow and Ncol of 2D-FBSE-EWT are set to 1 (as done in [16]).

The implementation of the methods was performed on MATLAB 2020a. The system's configuration is: Dell Optiplex 790 computer, equipped with Intel core i5 processor (3.20 GHz) and RAM of 14 GB.

Table VII illustrates the effect on the performance of the proposed framework at different cumulative variance of PCA, linear discriminant analysis (LDA) (first 30 linear components obtained by LDA) [39], and also when CLAHE is not applied on the proposed method (at 95% cumulative variance of PCA). It is clear from the table that the best performance with less number of features has been obtained at 95% cumulative variance, and CLAHE operation enhances the classification performance.

To check the utility of the proposed model, the trained DR grading classifier model is tested on a challenging APTOS-19 Kaggle database. The reason for choosing this database is that it is an Indian database and follows the same criteria for characterizing different grades of DR as done in the IDRiD. The pre-processing and all other steps are kept same as the IDRiD. The L and number of reduced features after PCA are 3 and 32, respectively. Fifty images from each grade are used to test the proposed DR model, and the SEN and SPE are shown in Table VIII. The Messidor database has been used to check the robustness of the proposed framework. The size of images in the database is unaltered. The same process is followed as was done for the IDRiD database. The L and number of features obtained after PCA (95% cumulative variance) are equal to 3 and 35, respectively. Table VIII shows the comparison of the proposed method for the IDRiD and Messidor database with existing methods. The results of the proposed method have shown significant improvement compared to existing methods. In IDRiD-2018

TABLE VII: Performance comparison of proposed methods at different cumulative variances of PCA, LDA and without CLAHE operation.

Performance measure	PCA (90%)		PCA (92%)		PCA (95%)		PCA (98%)		No PCA		LDA		No CLAHE	
	DR	DME	DR	DME	DR	DME	DR	DME	DR	DME	DR	DME	DR	DME
Features	25	26	26	28	30	30	98	98	360	360	30	30	30	30
ACY _{avg}	0.904	0.808	0.911	0.925	0.955	0.965	0.948	0.965	0.904	0.910	0.922	0.936	0.815	0.850

TABLE VIII: Comparison of proposed method with existing methods for Messidor, IDRiD, and APTOS-19 databases.

Database	Reference	DR		DME		JAC
		SEN	SPE	SEN	SPE	
Messidor	[3]	1	0.53	-	-	-
	[40]	0.91	-	-	-	-
	[41]	0.92	0.5	-	-	-
	[42]	-	-	0.75	0.91	-
	[1]	0.92	-	0.70	-	0.85
IDRiD	Proposed method	0.97	0.98	0.98	0.99	0.88
	[1]	-	-	-	-	0.65
APTO-19	Proposed method	0.83	0.95	-	-	-

challenge, JAC was used as an evaluation parameter and has provided a separate training and testing dataset for evaluation purpose. We followed the challenge description for comparing proposed methodology with existing works for IDRiD. In comparison table, for Messidor database, Chowdhury *et al.* [3] used Gaussian mix model, with KNN, SVM, and AdaBoost classifiers for DR grade diagnosis. Orlando *et al.* [40] used CNN and ensemble deep learning for DR grade diagnosis. Sanchez *et al.* [41] used blood vessel, red lesion, and bright lesion detection with KNN for DR grade diagnosis. Al-Bander *et al.* [42] utilized CNN to identify and extract features of DME automatically without any user intervention. For IDRiD, our method has out-performed the previous best method cross disease attention network (CANet) used for automatically diagnosing DR and DME. This is because our proposed methodology decomposes the image into subband images that highlight the lesion, which is responsible for DR and DME. The texture features are then extracted from those meaningful sub-images, which automatically enhance the classification performance, whereas there is no idea about what type of features are obtained by CANet to classify the different grades of DR and DME. Additionally, as the dimension of the features obtained by the proposed method is small, the doctors can use these features for diagnosis purposes, which is not possible in CNN-based approaches. CANet model used ResNet-50 as the backbone network (pre-trained network), so the image has to be resized (which is 350×350 followed by rescaling to 224×224) according to the input layer size of ResNet-50 which will degrade the resolution of the image and will affect the classification performance [10]. In contrast, in our case, the image resolution is unaltered to preserve all information present in the image. Another reason can be that the proposed methodology uses two separate models for training both the diseases. So if there is any chance of miss-classification by one model, it will not affect the performance of another model which improves the SEN and SPE of individual DR and DME grading problem. Finally, it will improve the overall

performance (JAC) of the proposed framework.

V. CONCLUSION

In this work, we have proposed a method to diagnose different grades of DR and DME simultaneously. Order-zero and order-one 2D-FBSE-FAWT are used to decompose images into subband images. Mean, standard deviation, median, entropy, kurtosis, and skewness of LBP and VAR histogram are used as a feature. Features are normalized, resampled, and then reduced using PCA. Total three simulations study were performed in this work. The first part of the simulation study was to choose the optimal value of parameters L , QF, DF, and RDY value to design a 2D-FBSE-FAWT filter-bank. ACY_{avg} was used as a performance measure in the simulation. For $L = 3$, QF = 3, DF = 0.5, and RDY = 1 the 2D-FBSE-FAWT filter-bank provided the best results. In the second part of the simulation study, the classification has been performed on 10-channel, 7-channel, and 3-channel subband grouping methods with previously selected parameters. 7-channel subband grouping method with RF classifier has given the best performance. In the third part of simulation study, the performance of order-zero and order-one 2D-FBSE-FAWT based methods are compared with different wavelets, x-lets, 2D-FBSE-EWT, transfer learning-based method, and without decomposition-based method. Order-zero 2D-FBSE-FAWT based method has shown the best performance. For IDRiD database ACY_{avg} for DR is 0.955, and for DME is 0.965. For Messidor database ACY_{avg} for DR is 0.975, and for DME is 0.985. A significant improvement of 4% and 3% have been found in JAC for IDRiD and Messidor database using order-zero 2D-FBSE-FAWT based method.

In future study, the proposed method can be used for the diagnosis of multi-class diseases using biomedical images. The limitation of 2D-FBSE-FAWT is that it is a constant QF decomposition method. So, this type of methods are not suitable when the signal has to be analyzed adaptively. 2D-FBSE-FAWT has used the advantage of FBSE for easy implementation of FAWT. It motivates us to use the FBSE spectrum in the future for image analysis.

REFERENCES

- [1] X. Li, X. Hu, L. Yu, L. Zhu, C. W. Fu, and P. A. Heng, “CANet: Cross-disease attention network for joint diabetic retinopathy and diabetic macular edema grading,” *IEEE Transactions on Medical Imaging*, vol. 39, no. 5, pp. 1483–1493, 2020.
- [2] S. Lizón-Martínez, R. Giannetti, J. Rodríguez-Marrero, and B. Tellini, “Design of a system for continuous intraocular pressure monitoring,” *IEEE Transactions on Instrumentation and Measurement*, vol. 54, no. 4, pp. 1534–1540, 2005.
- [3] S. Roychowdhury, D. D. Koozekanani, and K. K. Parhi, “Dream: diabetic retinopathy analysis using machine learning,” *IEEE Journal of Biomedical and Health Informatics*, vol. 18, no. 5, pp. 1717–1728, 2013.

- [4] M. U. Akram, A. Tariq, S. A. Khan, and M. Y. Javed, "Automated detection of exudates and macula for grading of diabetic macular edema," *Computer Methods and Programs in Biomedicine*, vol. 114, no. 2, pp. 141–152, 2014.
- [5] S. M. S. Islam, M. M. Hasan, and S. Abdullah, "Deep learning based early detection and grading of diabetic retinopathy using retinal fundus images," *International Conference on Machine Learning, Image Processing, Network Security and Data Sciences*, 2018.
- [6] Z. Lin, R. Guo, Y. Wang, B. Wu, T. Chen, W. Wang, D. Z. Chen, and J. Wu, "A framework for identifying diabetic retinopathy based on anti-noise detection and attention-based fusion," in *International Conference on Medical Image Computing and Computer-Assisted Intervention*. Springer, 2018, pp. 74–82.
- [7] F. Ren, P. Cao, D. Zhao, and C. Wan, "Diabetic macular edema grading in retinal images using vector quantization and semi-supervised learning," *Technology and Health Care*, vol. 26, no. S1, pp. 389–397, 2018.
- [8] A. M. Syed, M. U. Akram, T. Akram, M. Muzammal, S. Khalid, and M. A. Khan, "Fundus images-based detection and grading of macular edema using robust macula localization," *IEEE Access*, vol. 6, pp. 58784–58793, 2018.
- [9] J. Krause, V. Gulshan, E. Rahimy, P. Karth, K. Widner, G. S. Corrado, L. Peng, and D. R. Webster, "Grader variability and the importance of reference standards for evaluating machine learning models for diabetic retinopathy," *Ophthalmology*, vol. 125, no. 8, pp. 1264–1272, 2018.
- [10] H. Fu, J. Cheng, Y. Xu, D. W. K. Wong, J. Liu, and X. Cao, "Joint optic disc and cup segmentation based on multi-label deep network and polar transformation," *IEEE Transactions on Medical Imaging*, vol. 37, no. 7, pp. 1597–1605, 2018.
- [11] D. Parashar and D. Agrawal, "2-D compact variational mode decomposition-based automatic classification of glaucoma stages from fundus images," *IEEE Transactions on Instrumentation and Measurement*, vol. 70, pp. 1–10, 2021.
- [12] I. W. Selesnick, "Wavelet transform with tunable Q-factor," *IEEE Transactions on Signal Processing*, vol. 59, no. 8, pp. 3560–3575, 2011.
- [13] İ. Bayram, "An analytic wavelet transform with a flexible time-frequency covering," *IEEE Transactions on Signal Processing*, vol. 61, no. 5, pp. 1131–1142, 2012.
- [14] V. Gupta and R. B. Pachori, "Classification of focal EEG signals using FBSE based flexible time-frequency coverage wavelet transform," *Biomedical Signal Processing and Control*, vol. 62, p. 102124, 2020.
- [15] P. K. Chaudhary and R. B. Pachori, "Automatic diagnosis of glaucoma using two-dimensional Fourier-Bessel series expansion based empirical wavelet transform," *Biomedical Signal Processing and Control*, vol. 64, p. 102237, 2021.
- [16] ———, "FBSED based automatic diagnosis of COVID-19 using X-ray and CT images," *Computers in Biology and Medicine*, p. 104454, 2021.
- [17] R. Porter, "Robust rotation-invariant texture classification : wavelet, Gabor filter and GMRF based schemes," *IEE Proc. -Vis. Image Signal Process.*, vol. 144, no. 3, pp. 180–188, 1997.
- [18] S. S. R. Dhanushkodi and M. Vasuki, "Diagnosis system for diabetic retinopathy to prevent vision loss," *Applied Medical Informatics.*, vol. 33, no. 3, pp. 1–11, 2013.
- [19] M. A. Ali, T. Hurtut, T. Faucon, and F. Cheriet, "Glaucoma detection based on local binary patterns in fundus photographs," in *Medical Imaging 2014: Computer-Aided Diagnosis*, vol. 9035. International Society for Optics and Photonics, 2014, p. 903531.
- [20] S. Morales, K. Engan, V. Naranjo, and A. Colomer, "Retinal disease screening through local binary patterns," *IEEE Journal of Biomedical and Health Informatics*, vol. 21, no. 1, pp. 184–192, 2015.
- [21] M. Garnier, T. Hurtut, H. B. Tahar, and F. Cheriet, "Automatic multiresolution age-related macular degeneration detection from fundus images," in *Medical Imaging 2014: Computer-Aided Diagnosis*, vol. 9035. International Society for Optics and Photonics, 2014, p. 903532.
- [22] P. Porwal, S. Pachade, R. Kamble, M. Kokare, G. Deshmukh, V. Sahasrabuddhe, and F. Meriaudeau, "Indian diabetic retinopathy image dataset (IDRiD): A database for diabetic retinopathy screening research," *Data*, vol. 3, no. 3, 2018.
- [23] E. Decencière, X. Zhang, G. Cazuguel, B. Laÿ, B. Cochener, C. Trone, P. Gain, J.-R. Ordóñez-Varela, P. Massin, A. Erginay, B. Charton, and J.-C. Klein, "Feedback on a publicly distributed image database: the messidor database," *Image Analysis and Stereology*, pp. 231–234, 2014.
- [24] G. Mohan P., C. Prakash, and S. V. Gangashetty, "Bessel transform for image resizing," in *2011 18th International Conference on Systems, Signals and Image Processing*, 2011, pp. 1–4.
- [25] J. Schroeder, "Signal processing via Fourier- Bessel series expansion," *Digital Signal Processing*, vol. 3, pp. 112–124, 1993.
- [26] K. Gopalan, T. R. Anderson, and E. J. Cupples, "A comparison of speaker identification results using features based on cepstrum and Fourier-Bessel expansion," *IEEE Transactions on Speech and Audio Processing*, vol. 7, no. 3, pp. 289–294, 1999.
- [27] R. B. Pachori and P. Sircar, "EEG signal analysis using FB expansion and second-order linear TVAR process," *Signal Processing*, vol. 88, no. 2, pp. 415–420, 2008.
- [28] V. P. Shah, N. H. Younan, S. S. Durbha, and R. L. King, "A systematic approach to wavelet-decomposition-level selection for image information mining from geospatial data archives," *IEEE Transactions on Geoscience and Remote Sensing*, vol. 45, no. 4, pp. 875–878, 2007.
- [29] T. Ojala, M. Pietikainen, and T. Maenpaa, "Multiresolution gray-scale and rotation invariant texture classification with local binary patterns," *IEEE Transactions on Pattern Analysis and Machine Intelligence*, vol. 24, no. 7, pp. 971–987, 2002.
- [30] S. Zhang, X. Li, M. Zong, X. Zhu, and D. Cheng, "Learning k for knn classification," *ACM Transactions on Intelligent Systems and Technology (TIST)*, vol. 8, no. 3, pp. 1–19, 2017.
- [31] R.-E. Fan, P.-H. Chen, C.-J. Lin, and T. Joachims, "Working set selection using second order information for training support vector machines," *Journal of Machine Learning Research*, vol. 6, no. 12, 2005.
- [32] V. F. Rodriguez-Galiano, B. Ghimire, J. Rogan, M. Chica-Olmo, and J. P. Rigol-Sánchez, "An assessment of the effectiveness of a random forest classifier for land-cover classification," *ISPRS Journal of Photogrammetry and Remote Sensing*, vol. 67, pp. 93–104, 2012.
- [33] I. Daubechies, *Ten lectures on wavelets*. SIAM, 1992.
- [34] I. W. Selesnick, R. G. Baraniuk, and N. C. Kingsbury, "The dual-tree complex wavelet transform," *IEEE Signal Processing Magazine*, vol. 22, no. 6, pp. 123–151, 2005.
- [35] R. R. Coifman and M. V. Wickerhauser, "Entropy-based algorithms for best basis selection," *IEEE Transactions on information theory*, vol. 38, no. 2, pp. 713–718, 1992.
- [36] D. L. Donoho, "Wedgelets: Nearly minimax estimation of edges," *The Annals of Statistics*, vol. 27, no. 3, pp. 859–897, 1999.
- [37] E. Candes, L. Demanet, D. Donoho, and L. Ying, "Fast discrete curvelet transforms," *multiscale modeling & simulation*, vol. 5, no. 3, pp. 861–899, 2006.
- [38] M. N. Do and M. Vetterli, "The contourlet transform: an efficient directional multiresolution image representation," *IEEE Transactions on image processing*, vol. 14, no. 12, pp. 2091–2106, 2005.
- [39] A. Tharwat, T. Gaber, A. Ibrahim, and A. E. Hassanien, "Linear discriminant analysis: A detailed tutorial," *AI communications*, vol. 30, no. 2, pp. 169–190, 2017.
- [40] J. I. Orlando, E. Prokofyeva, M. Del Fresno, and M. B. Blaschko, "An ensemble deep learning based approach for red lesion detection in fundus images," *Computer Methods and Programs in Biomedicine*, vol. 153, pp. 115–127, 2018.
- [41] C. I. Sánchez, M. Niemeijer, A. V. Dumitrescu, M. S. Suttorp-Schulten, M. D. Abramoff, and B. van Ginneken, "Evaluation of a computer-aided diagnosis system for diabetic retinopathy screening on public data," *Investigative Ophthalmology & Visual Science*, vol. 52, no. 7, pp. 4866–4871, 2011.
- [42] B. Al-Bander, W. Al-Nuaimy, M. A. Al-Taee, B. M. Williams, and Y. Zheng, "Diabetic macular edema grading based on deep neural networks," 2016.